Optics and Laser Technology 131 (2020) 106408

Contents lists available at ScienceDirect

Optics and Laser Technology

journal homepage: www.elsevier.com/locate/optlastec

Full length article

The role of pulse repetition rate on picosecond pulsed laser processing of Zn and Zn-coated steel

H. Mustafa[a,*], D.T.A. Matthews[a,b], G.R.B.E. Römer[a]

[a] Chair of Laser Processing, Department of Mechanics of Solids, Surfaces & Systems (MS^3), Faculty of Engineering Technology, University of Twente, Enschede, the Netherlands

[b] Chair of Skin Tribology, Department of Mechanics of Solids, Surfaces & Systems (MS^3), Faculty of Engineering Technology, University of Twente, Enschede, the Netherlands

HIGHLIGHTS

- MRR is defined by pulse energy and number of pulses than average power.
- MRR increases for heat accumulation and ablated depth decreases for particle shielding.
- Heat accumulation is higher in bulk zinc than in Zn-coated sample.
- Steel substrate acts as a heat sink inhibiting a higher degree of heat accumulation.

ARTICLE INFO

Keywords:
Ultrashort pulsed laser
Pulse repetition rate
Polycrystalline zinc
Galvanized steel
Material removal rate

ABSTRACT

Zinc and zinc-coated steel is processed with a picosecond laser source at a wavelength of 1030 and 515 nm to investigate the effect of time between consecutive pulses, i.e. pulse repetition rate on the laser ablation efficiency, in terms of maximum achievable depth of the ablated crater, material removal rate and processing quality. With increasing pulse repetition rate up to 40 kHz and number of pulses on the same location, material removal rate increases due to heat accumulation, while the maximum achievable depth decreases due to particle shielding for both zinc and zinc coated steel. It was found that, unlike the zinc-coated sample, both material removal rate and achievable depth is enhanced for bulk zinc at high repetition rates, due to a greater degree of heat accumulation than particle shielding. Using a numerical heat flow model, it is shown that the difference between bulk zinc and zinc-coated steel stems from the steel substrate that effectively acts as a heat sink for the absorbed energy in the zinc coating, inhibiting a higher degree of heat accumulation.

1. Introduction

Surface texturing using ultrashort-pulsed laser sources is an emerging industrial-scale processing technique [1,2]. Depending on the application, texture requirements generally incorporate shape geometry, packing density and product quality (i.e. roughness, defects, redepositions etc.). Therefore, productivity of the laser surface texturing process depends on achievable depth, material removal rate and ablated surface quality. Removal rate is directly proportional to the maximum ablated depth. For a given depth, material removal rate can be enhanced by increasing either the laser fluence F_0 or the pulse repetition rate f_p. Increasing pulse energy E_p or decreasing laser beam radius ω_0 results in an increase in fluence ($F_0 = 2{\cdot}E_p/\pi\omega_0^2$). The specific removal rate is found to peak at an optimum fluence related to the threshold fluence at which ablation occurs as $F_{opt} = e^2{\cdot}F_{th}$ [3,4]. As the pulse duration shortens, specific removal rate saturates at the maximum for $F_0 \geqslant F_{opt}$ [5]. Since laser fluence is inversely proportional to the square of the beam radius at a given pulse energy, the laser fluence can be optimized by changing the laser spot radius, e.g., by expanding/reducing the laser spot diameter before focusing optics, and/or, processing the substrate with a defocused beam. Typically, commercially available ultrashort pulsed laser sources can deliver pulses with a maximum pulse energy at kHz repetition rates, whereas E_p generally decreases at MHz repetition rates [6]. Therefore, even at maximum pulse energy, fluence can be controlled by off-focus processing, i.e. increasing beam radius ω_0, while using full energy per pulse delivered by the laser source. Conversely, if multiple beam processing is employed, by splitting a single high energy beam into several parallel beams, the beam diameter could be adjusted

* Corresponding author.
E-mail address: h.mustafa@utwente.nl (H. Mustafa).

https://doi.org/10.1016/j.optlastec.2020.106408
Received 30 August 2019; Received in revised form 10 May 2020; Accepted 3 June 2020

at reduced energy per pulse in the splitted beams to achieve maximum removal rate. On the other hand, increasing pulse repetition rate f_p, i.e. decreasing time between consecutive pulses $t_p = \frac{1}{f_p}$, results in lesser time for the residual heat from the previous laser pulses to dissipate, as well as the ablated particles to disperse away from the laser material interaction zone. As a consequence, heat accumulation takes place in the target material and particle shielding (partially) blocks the incident laser beam from reaching the target surface [7,8]. At high repetition rates, heat accumulation dominates over particle shielding [9,10]. With increasing fluence and/or number of pulses and/or geometrical pulse-to-pulse overlap, the observed enhancement in heat accumulation affects the ablation threshold and incubation coefficient [11,12,6]. Inevitably, heat accumulation affects the morphology of the irradiated area through the formation of different micro-features in the ablated crater [13,14], rim formation around the crater [10] and heat affected zone (HAZ) [15]. As a result, the quality of processing, in terms of visual appearance, surface roughness etc., also varies with pulse repetition rate, depending on the target material [16–18]. To reduce the thermal load on the sample, fast beam deflection and/or multiple beam-splitting (e.g. diffractive optical elements (DOE), spatial light modulators (SLM)) becomes a preferred processing route, however, technical limitations like maximum achievable beam deflection velocity, flexibility and damage threshold of beam-splitting elements imposes a bottleneck [19–21].

From the point of global production and consumption, zinc is the fourth most used metal worldwide after iron, aluminium and copper [22]. For its excellent corrosion resistance and cathodic protection property, 60% of the globally produced zinc is used for galvanizing to prolong the service life of steel [23]. On the other hand, 35% of the globally produced zinc is used for alloying [23]. Therefore, Zn is seldom used in its pure form. Ultrashort-pulsed laser processing of zinc is mainly performed in the framework of pulsed laser ablation in liquid (PLAL) in order to produce nanoparticles, laser induced breakdown spectroscopy (LIBS), pulsed laser deposition (PLD) and laser induced forward transfer (LIFT) [24,25]. Generally, low repetition rates are preferred for LIBS, PLD and LIFT for better control over the end result. Substantial increase in the productivity of nanoparticle generation with increasing repetition rate was reported for a number of metals (Pt, Au, Ag, Al, Cu, Ti, Steel) in PLAL [26,27]. Also, the effect of pulse repetition rate in air has been studied substantially [9,10,15,28,16,29,18,21,19,20,30,6,17,31] for a variety of materials. However, no work regarding the role of pulse repetition rate has been reported for zinc or zinc-coated steel in air.

In this work, we present the effect of pulse repetition rate on the maximum achievable depth, material removal rate and processing quality of Zn and Zn-coated steel using a picosecond pulsed laser source at its fundamental (1030 nm) and second harmonic (515 nm) wavelengths. The morphology and the dimensional features are analyzed by means of confocal laser scanning microscopy. Ablation fluence threshold and energy penetration depth are determined for low number of laser pulses at different pulse repetition rates. The material removal rate, achievable depth and processing quality in terms of rim formation is assessed in order to determine the optimum processing parameters at the maximum pulse energy of the laser source. Moreover, a numerical heat flow model is presented to account for the changes induced by pulse repetition rate in the picosecond-pulsed laser ablation of zinc and zinc-coated steel.

2. Experimental setup

2.1. Laser setup

The laser ablation experiments were performed under atmospheric conditions in a cleanroom environment, using a diode pumped thin disc Yb:YAG pulsed laser source (TruMicro 5050 of Trumpf GmbH, Germany). This source emits 6.7 ps laser pulses of linearly polarized light and shows a nearly Gaussian power density profile ($M^2 < 1.3$). In this work, p-polarized light at both the central (1030 nm) and the second harmonic (515 nm) wavelengths was used. A galvo-scanner (IntelliScan14 of ScanLab GmbH, Germany), equipped with a telecentric flatfield F-theta-Ronar lens (Linos GmbH, Germany) was used to scan the focused laser beam over the surface of the sample. The sample was placed in the focal plane. The focal spot radius was measured from the fluence profile using a charge-coupled device (CCD) sensor-based, beam diagnostic system (MicroSpot Monitor of Primes GmbH, Germany). The setup related parameters are listed in Table 1.

Table 1
Laser setup parameters.

Parameters	Laser wavelength [nm]	
	1030	515
Focal length [mm]	80	100
Focal spot radius [μm]	14.6 ± 1.6	12.0 ± 0.5
Ellipticity @ focus	0.89	0.81
Max. pulse energy [μJ]	135	82
Min. pulse energy [μJ]	3	1

The beam impinges perpendicular to the sample surface. The focus position was fixed for all the experiments and coincided with the original surface. The experiments were performed in percussion drilling mode. The number of pulses at a given pulse repetition rate was controlled by electronically gating the laser source using real time interface with a switching delay of 10 μs. The emitted number of pulses within the gating time was verified using a high-speed Si photodiode (DET10A/M of Thorlabs, USA) in combination with a GHz oscilloscope (LeCroy WavePro 7000A of Teledyne Technologies, Inc., USA). Apart from a transverse air flow to protect the F-theta-Ronar lens, no shielding gas was used to suppress/extract debris from the laser material interaction zone during processing. The laser energy supplied to the surface was varied by using a combination of a half-wave plate and a polarizing beam splitter. A pyroelectric detector (PM30 with FieldMax II of Coherent, USA) was used to measure the average laser power incident on the sample with an error less than 8%. The energy of the individual pulses was determined by dividing the measured average laser power by the pulse frequency applied. The power instability of the laser source is less than 2%. The pulse repetition rate was varied from 40 Hz to 400 kHz. Therefore, the time between consecutive pulses on the same location was varied between 2.5 μs to 25 ms. The geometrical pulse-to-pulse distance was at least 125 μm and the number of pulses varied from $N = 4$ to 40 with an uncertainty (due to the switching delay in the gating of the laser source) of an additional pulse, i.e. $N = 4(+1)$ to $40(+1)$. A minimum of 10 craters were created per laser setting to ensure statistically sound values in measured quantities.

2.2. Material

In this work, bulk and coated zinc samples were used. Bulk polycrystalline zinc (Zn) samples were typical zinc (99.7%wtZn, 0.3%wtAl), which is typically used for coating on steel products, and prepared as reported in [25,24]. Coated zinc samples were galvanized steel, having a Zinc coating (99.7%Zn, 0.3%Al) weight of 70 g/m^2 (average thickness of 8 ± 2 μm), deposited by Hot Dip Galvanizing (HDG) process on Titanium Stabilized Ultra Low Carbon (TiSULC) steel substrate. The average roughness (R_a) of the bulk and coated samples were 0.03 and 0.5 μm respectively. Bulk and coated Zn samples were cleaned using ethanol (>99%) and Ammonia (<5%) solution ($NH_3(aq)$) prior to and after the ablation experiments respectively.

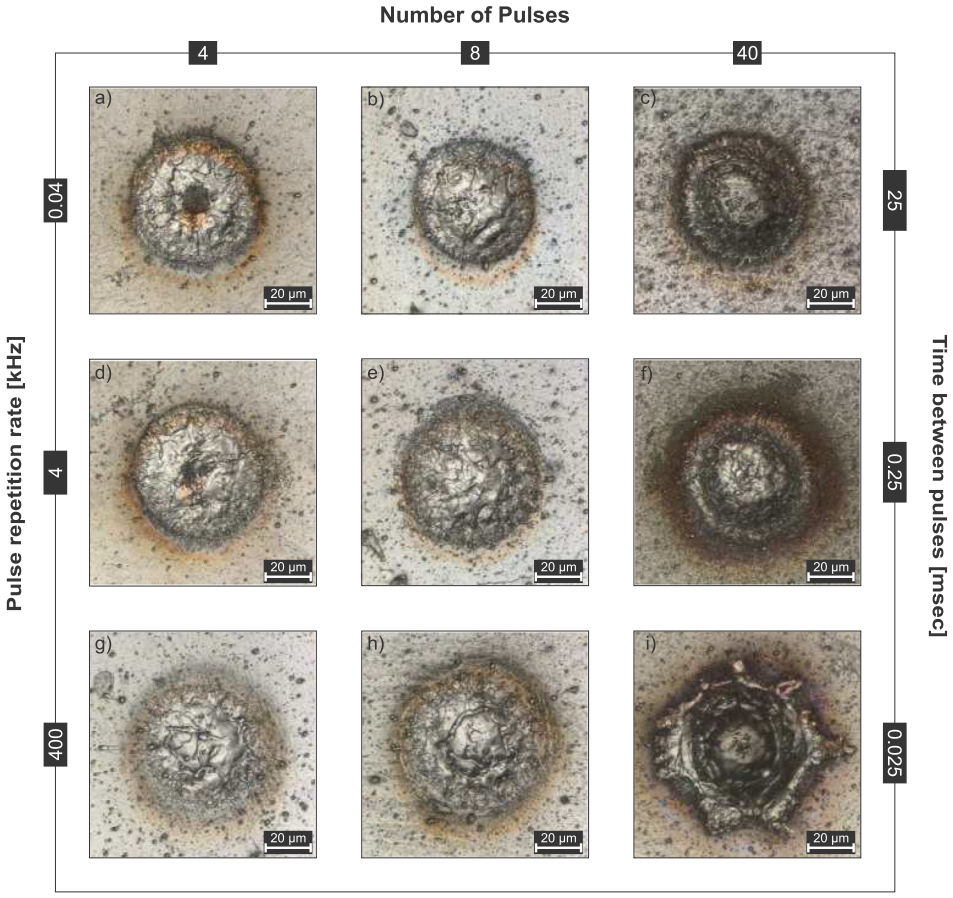

Fig. 1. Confocal images of bulk zinc surface irradiated at 1030 nm at different pulse repetition rates f_p (rows) and at different number of laser pulses N(columns) at a peak fluence of $F_0 = 40\ \mathrm{J/cm^2}$.

2.3. Analysis tools

The roughness of samples after surface treatments, as well as the laser-induced surface profiles (the latter referred to as "craters" here), were measured by means of Confocal Laser Scanning Microscopy (CLSM), (VK-9700 of Keyence Corporation, Japan). The lateral and vertical resolution of CLSM measurements was 276 nm and 1 nm respectively. CLSM images were analyzed with the help of a image processing algorithm using a MATLAB script [32] to measure the dimensional features of the craters.

2.4. Calculation method

From the CLSM measurements, the ablated volume at different laser processing parameters were calculated along with the diameter and the depth of ablated craters. For a laser beam with a Gaussian fluence distribution, the ablated volume per pulse can be expressed as [4,3]

$$\Delta V = \frac{1}{4}\cdot\pi\cdot\omega_{maj}\cdot\omega_{min}\cdot\delta_e\cdot\left[\ln\left(\frac{F_0}{F_{th}}\right)\right]^2, \tag{1}$$

where δ_e and F_{th} are fit parameters for energy penetration depth and ablation threshold fluence respectively. The peak fluence F_0 is related to pulse energy $E_p$as $F_0 = (2\cdot E_p)/(\pi\cdot\omega_{maj}\cdot\omega_{min})$, where ω_{maj} and ω_{min} are the laser beam radius ($1/e^2$) along the major and minor axes respectively. Two ablation regimes, as mentioned in [24], are demarcated at $F_0 \leqslant 10\ \mathrm{J/cm^2}$ and denoted as regime I and II respectively. The non-linear least squared fit of Eq. (1) was applied in regime I only.

Material removal rate is generally determined by varying the pulse repetition rate at maximum average power P_{avg} of the laser source used and is given by [4,33,30]

$$MRR = \frac{\Delta V\cdot f_p}{P_{avg}}\ \mathrm{m^3/(s\cdot W)}, \tag{2}$$

where ΔV is the ablated volume per pulse calculated from Eq. (1). This method is beneficial for taking the full benefit of the laser source [34,21] - i.e. when exploiting the maximum average power. However, the (maximum) pulse energy of most laser sources is generally constant up to pulse frequencies in the MHz regime. For higher pulse repetition rates, the pulse energy drops [6]. Therefore, at an constant average output power, increasing repetition rate decreases the energy per pulse. Moreover, in a given time period, it is obvious that a higher number of pulses are emitted at higher repetition rate. In order to make a fairer comparison between the pulse energy, number of pulses and time between consecutive pulses, the material removal rate (MRR), in this work, is defined as

$$MRR = \frac{V}{E_p\cdot t_{process}}\ \mathrm{m^3/(J\cdot s)}, \tag{3}$$

where $V$is the ablated volume, E_p is the pulse energy, and the processing time $t_{process}$ is defined as

$$t_{process} = (N-1)\cdot\frac{1}{f_p} + \tau_p, \tag{4}$$

where, N is number of pulses on the same location and τ_p is laser pulse duration and $\frac{1}{f_p}$ is time between consecutive pulses.

3. Results

In the following, first we discuss the results obtained during processing of bulk Zn samples in Section 3.1 processed at a wavelength of

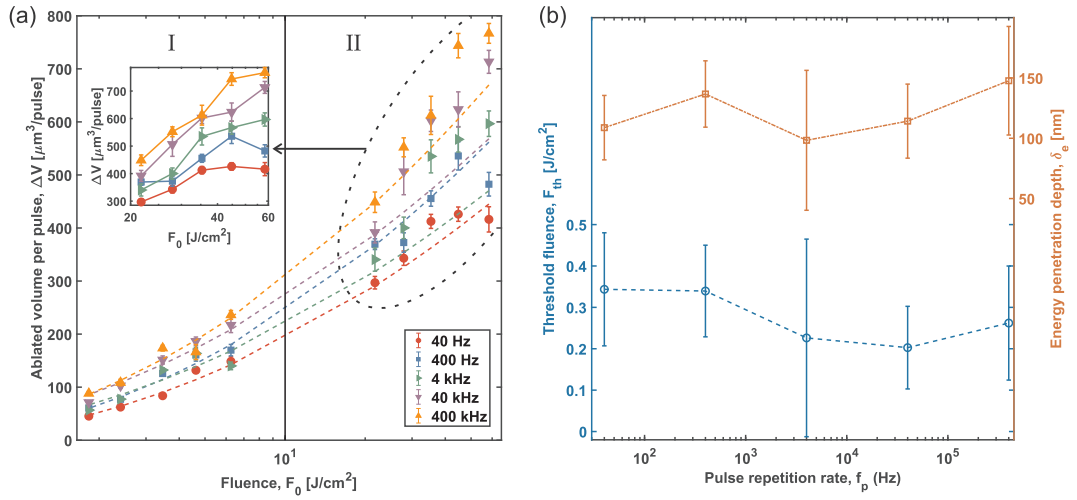

Fig. 2. (a) Ablated volume per pulse ΔV of bulk zinc processed at a wavelength of 1030 nm as a function of peak fluence F_0 for $N = 4$ at different pulse repetition rates. The dashed curves represent the least squared fit according to Eq. (1) in regime I only. These curves were extended into regime II. Note that the error bars are smaller than the markers of the data points. Inset shows the data points in regime II, where lines are guides for the eye only. (b) Threshold fluence, $F_{th}(4)$ and energy penetration depth $\delta_e(4)$ as a function of pulse repetition rate f_p.

1030 nm. Next in Section 3.2, the results of Zn-coated steel, processed at a wavelength of 515 nm, are presented.

3.1. Bulk zinc

Fig. 1 shows the confocal images of the bulk zinc sample processed at a wavelength of 1030 nm at different pulse repetition rates f_p and number of pulses N. With increasing f_p at any given number of pulses, the differences in crater morphology are found primarily in the heat affected zone and as melt displacement. This is because the time between consecutive pulses t_p decreases with increasing pulse repetition rate (see Fig. 1)). For a decrease in t_p by a factor of 100 (from $t_p = 25$ ms to 0.25 ms), a heat affected zone (HAZ) is observed around the crater (see Fig. 1(f)), which is not observed at lower repetition rates around the crater (see Fig. 1(c)). If t_p is decreased further by a factor of 1000 (from $t_p = 25$ ms to 0.025 ms), the HAZ is almost covered by the rim formed by the displaced melt (see Fig. 1(i)).

The ablated volume per pulse ($N = 4$) for different pulse repetition rates are plotted against the laser peak fluence F_0 in Fig. 2(a). The vertical line at 10 J/cm^2 demarcates the two ablation regimes mentioned in previous works [25,24]. The dashed curves in Fig. 2(a) represent nonlinear least squared fit of Eq. (1) for regime I. As can be observed in the inset, the data points above 10 J/cm^2 cannot be explained by Eq. (1) regardless of the pulse repetition rates. In regime II, a saturation in ablated depth was reported for $t_p = 4.9$ ms in a previous work [24]. However, this saturation behavior of the ablated volume at high fluence levels diminishes as the time between pulses t_p decreases - i.e. as the pulse repetition rate increases (see inset of Fig. 2(a)). In Fig. 2(b), the fit parameters of Eq. (1), i.e. δ_e and F_{th} are plotted against the pulse repetition rate. The decrease in F_{th} or the increase in δ_e, with increasing f_p, is not that significant at low number of pulses.

Fig. 3(a) shows the material removal rates (MRR), according to Eq. (3), at the maximum available pulse energy from the laser source. For a given number of pulses, MRR gradually increases with increasing f_p. As can be observed from Fig. 3(b), the crater depth experiences a sharp increase at $f_p = 400$ kHz for any given number of pulses. This observation indicates that considerable heat accumulation takes place when $t_p = 25$ µs. In Fig. 3(c), the rim volume is plotted against the pulse repetition rate. Except for $N = 4$, rim volume decreases with increasing f_p up to 40 kHz and then increases steeply for increasing f_p. A higher rim volume indicates that more material has been redeposited around the crater at $f_p = 400$ kHz than any other pulse repetition rates.

Fig. 4 shows cross-sections of normalized (i.e. $\frac{h(r)}{h_{max}}$) crater profiles, obtained from CLSM measurements, at 40.75 J/cm^2 at different pulse repetition rates for different number of pulses. Fig. 4(a) shows that, at $N = 4$, no significant difference is observable in the depth profiles except for $f_p = 400$ kHz. As the number of pulses increases, craters processed at $f_p = 400$ Hz result in deeper craters than craters processed at $1\,\text{kHz} < f_p \leqslant 40\,\text{kHz}$ (see Fig. 4(b)–(d)). On the other hand, craters processed at $1\,\text{kHz} < f_p \leqslant 40\,\text{kHz}$ exhibit a negligible rim around the crater compared to $f_p \leqslant 1\,\text{kHz}$ and $f_p = 400$ kHz. The rim around the crater in Fig. 4 is marked by dashed black circles. In any case, craters processed at $f_p = 400$ kHz have the largest ablated depth than any other pulse repetition rates.

3.2. Zinc-coated steel

Fig. 5 shows the confocal images of the zinc coated steel, i.e. galvanized steel, samples processed at a wavelength of 515 nm at the maximum pulse energy of the source. Dendritic depressions (due to production method) and grain boundaries cover the untreated surface and results in an average surface roughness that is 16 times higher than of the bulk polished zinc samples (see Section 2.2). The effect of pulse repetition rate is readily observable after the surface has been irradiated with $N = 4$ as shown in Fig. 5(a) and (c). In Fig. 5(a), the crater morphology features a deep central modified zone surrounded by a surface modification zone followed by a surface (de) coloration zone. On the contrary, the demarcation between the melt-dominated central modified zone and the surface modification zone is more gradual when the pulse repetition rate is increased by three orders of magnitude from 40 Hz to 40 kHz (see Fig. 5(b)). At $N = 40$, the central modified zone, where the substrate steel is exposed, is the dominant feature of the crater, whereas the Zn coating around the crater features surface modification zone followed by surface (de) coloration (see Fig. 5(b) and (d)). When the time between consecutive pulses is longer, the central part of the exposed steel substrate appears drilled (see Fig. 5(b)). On the other hand, the central part is melt-dominated when the time between consecutive pulses is shorter (see Fig. 5(d)).

At any pulse repetition rate, the maximum ablated depth for $N = 4$ was about 6 ± 1 µm. If the number of pulses are increased further, the crater depth is near or even exceeds the coating thickness (see Fig. 7(b)). It should be noted that the heat diffusion is affected as the coating layer thickness is reduced. However, the remaining coating layer thickness, at a crater depth of 6 µm, is large enough to exclude it

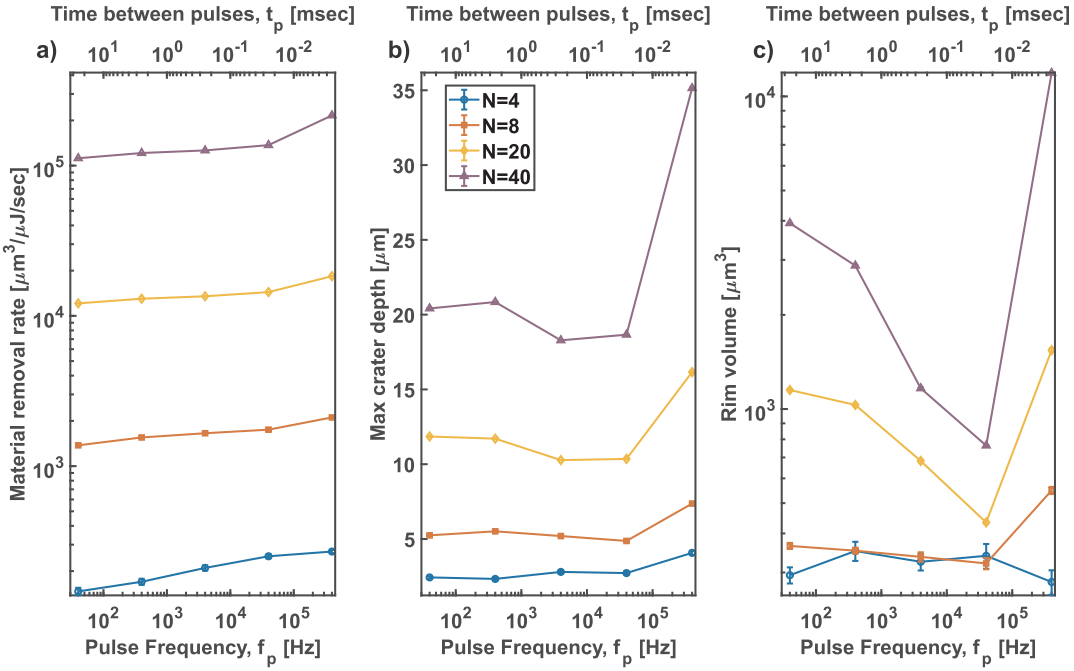

Fig. 3. (a) Material removal rate (MRR) according to Eq. (3) at E_p = 135 μJ, (b) maximum crater depth and (c) rim volume of bulk Zn processed at a wavelength of 1030 nm as a function of pulse repetition rate for F_0 = 40 J/cm². Curves are a guide for the eye.

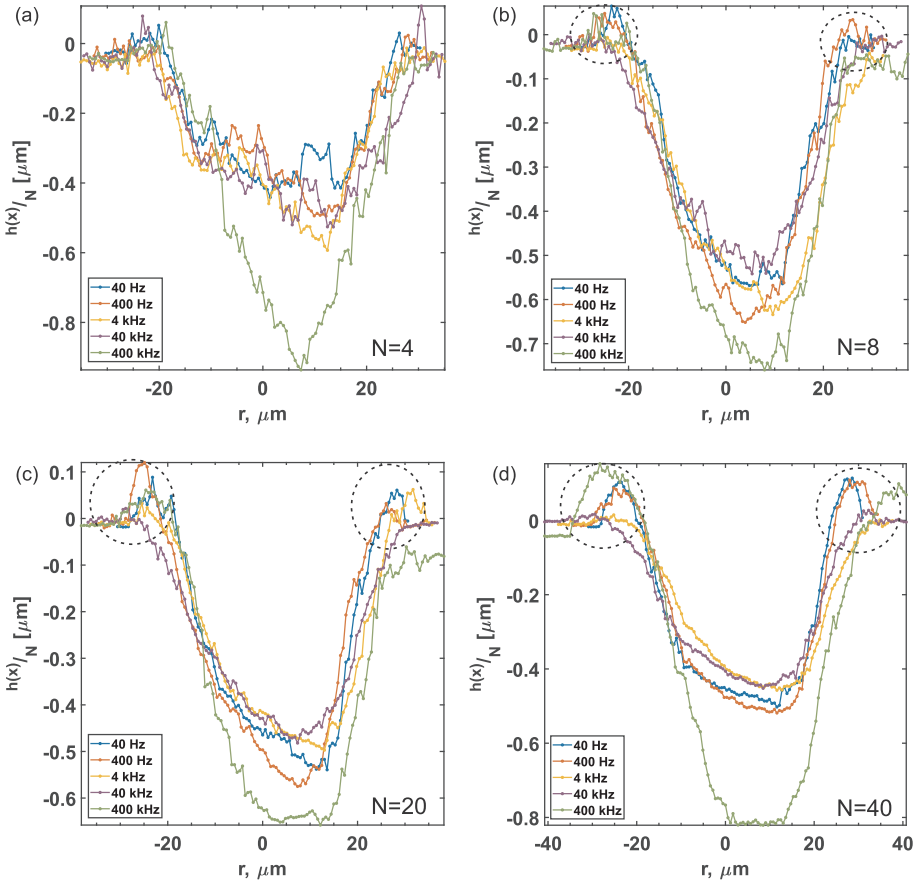

Fig. 4. Cross-sections (obtained from CLSM measurements) of ablated craters on the surface of bulk zinc normalized by corresponding number of pulses *N*at E_p = 135 μJ, F_0 = 40 J/cm² and a wavelength of 1030 nm. The dashed circle in the graphs represents rim around the crater.

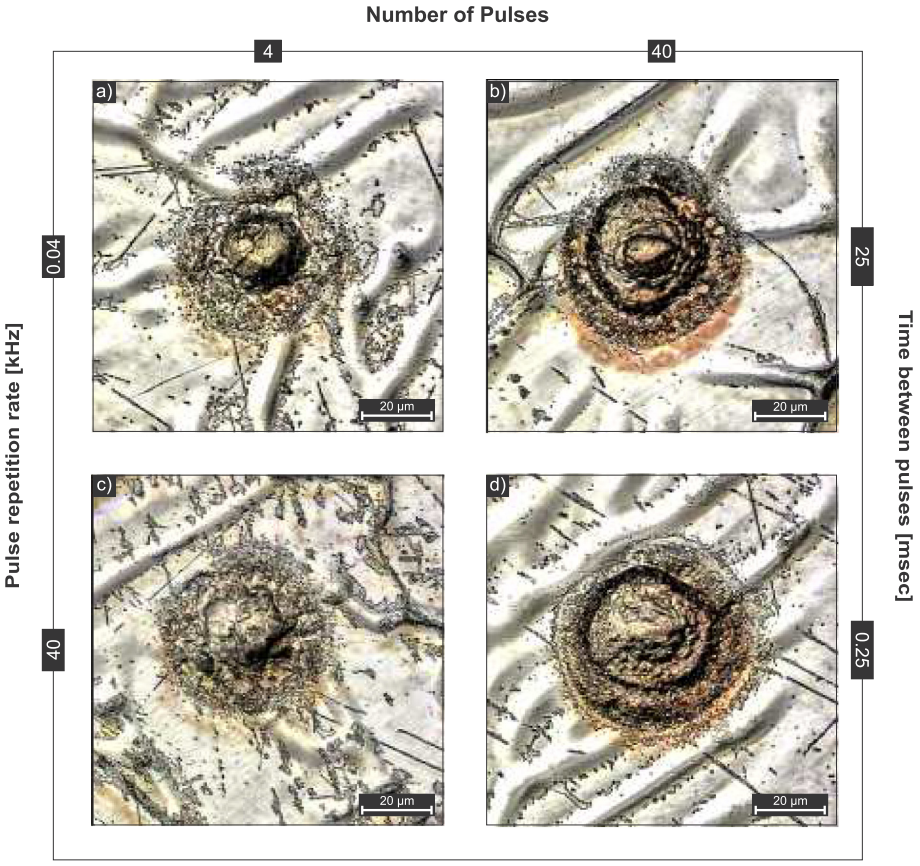

Fig. 5. Confocal images of galvanized steel surface irradiated at different pulse repetition rate f_p (rows) and at different number of laser pulses N (columns) at peak fluence $F_0 = 40\ \mathrm{J/cm^2}$.

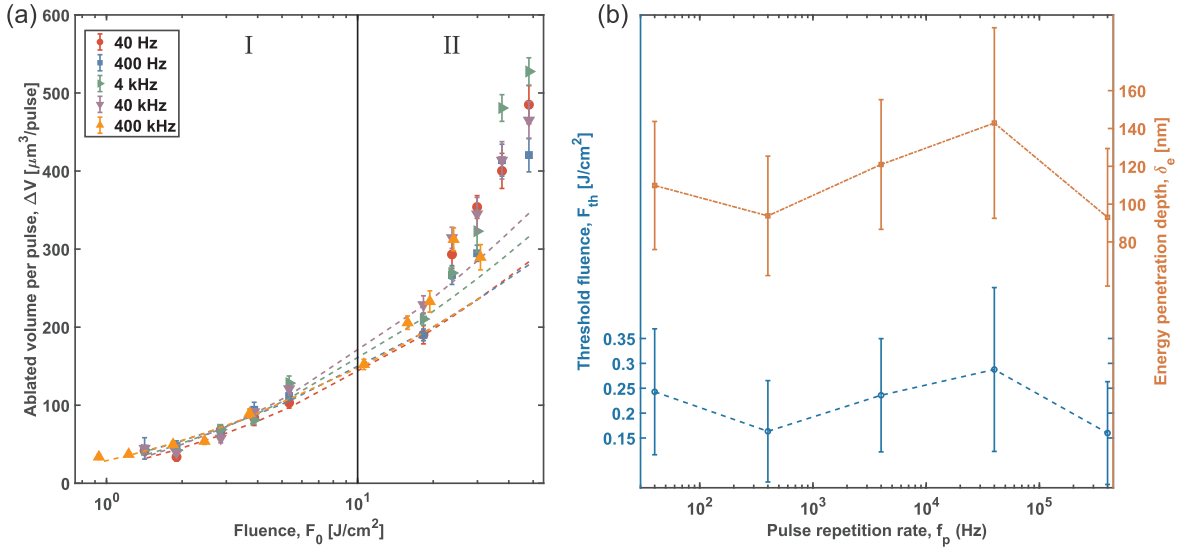

Fig. 6. (a) Ablated volume per pulse ΔV of galvanized steel processed at a wavelength of 515 nm as a function of peak fluence F_0 for $N = 4$ at different pulse repetition rates. The dashed curves represent the least squared fit according to Eq. (1) in regime I only and extended in regime II. Note that the error bars are smaller than the data points. (b) Threshold fluence, $F_{th}(4)$ and energy penetration depth $\delta_e(4)$ as a function of pulse repetition rate f_p.

as thin film. Assuming that the ablated material is solely zinc, the ablated volume per pulse is plotted in Fig. 6(a) as a function of peak fluence for different pulse repetition rate at $N = 4$. As can be seen from this figure, data points in regime II cannot be explained by the fit of Eq. (1) shown by the dashed curves. The lower fluence value for $f_p = 400$ kHz is due to the reduction in conversion efficiency of the SHG crystal at high pulse energy and high repetition rate of our SHG unit. Similar to the bulk zinc sample, the change in threshold fluence and energy penetration depth with increasing pulse repetition rate is not significant, as shown in Fig. 6(b).

The material removal rate (MRR), according to Eq. (3), of galvanized steel samples at the maximum pulse energy of the laser source is shown in Fig. 7(a). Similar to bulk zinc samples, *MRR*increases with increasing pulse frequency. However, the maximum crater depth shows

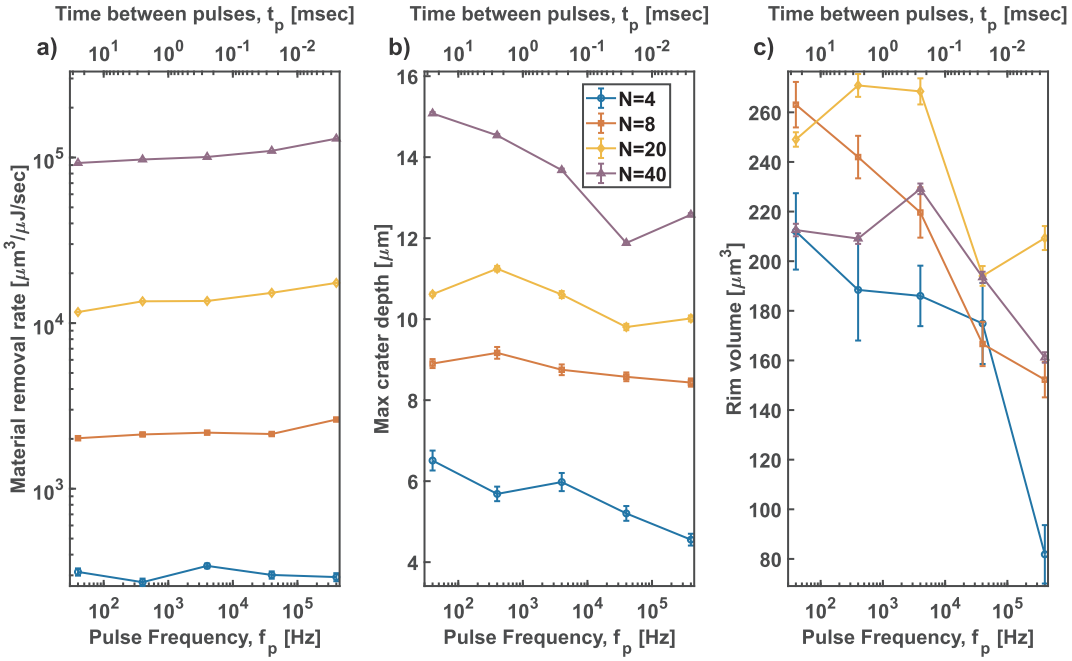

Fig. 7. (a) Material removal rate (MRR) according to Eq. (3), (b) maximum crater depth and (c) rim volume of galvanized steel processed at a wavelength of 515 nm as a function of pulse repetition rate for $F_0 = 40.\ \mathrm{J/cm^2}$.

opposite trend than *MRR*(see Fig. 7(b)). The crater depth is maximum when the time between pulses is longest at a given *N*. As can be seen from Fig. 7(b), this observation is true when the crater depth is either in zinc coating ($N = 4$) or in the steel substrate ($N = 40$). Otherwise, at the coating-substrate interface, the peak in the maximum ablated crater depth shifts towards 400 Hz (see the curves for $N = 8$ and 20 in Fig. 7(b)). An increase in *MRR*, when the maximum crater depth decreases, indicates that the crater dimensions increase laterally rather than vertically. This is expected as the difference in melting temperature of Zn ($T_m = 692.68$ K) and forming steel ($T_m = 1803$ K) is significant.

The evolution of the crater shape in the coating and in the substrate for increasing number of pulses can be visualized from the cross-section of the crater, obtained from CLSM measurements, as shown in Fig. 8. The dashed horizontal line in Fig. 8(b)-(d) indicates the coating-substrate interface. For $N = 4$, higher pulse repetition rates result in lower crater depth (see Fig. 8(a)). Also, the craters are within the coating layer. As the number of pulses are increased, the maximum crater depth is at or near the coating-substrate interface and the differences in the crater shape are hard to distinguish (see Fig. 8(b) and (c)). When the crater is well within the steel substrate, the differences in the crater shapes become apparent. As can be observed in Fig. 8(d), craters processed at low pulse repetition rate are deeper, while the shape of the crater gets wider in the coating layer as the pulse repetition rate increases. The rim around the craters is not as extensive as the bulk zinc samples. While the maximum rim height is 10 μm for bulk Zn samples, the rims are less than a micron high in galvanized steel samples, resulting in two order of magnitude lower rim volume than bulk zinc (compare to Fig. 7(c)).

4. Discussion

As the pulse repetition rate increases, time between consecutive pulses on the same location decreases to such an extent that each additional pulse reaches the target surface before full dissipation of residual heat into the bulk [35] and/or before the lifetime of the ablation plume, present within the beam path, ends [8]. As can be observed from Fig. 3(b), the reduction in maximum crater depth around 40 kHz gets pronounced with increasing number of pulses indicating an increased degree of shielding of the laser beam by the particles. At 400 kHz, the achievable depth increases drastically, indicating heat accumulation overcomes particle shielding [9]. Bauer et al. modeled the spatial and temporal temperature distribution $T(x, y, z, t)$ in a solid material due to a spatial Gaussian shaped stationary laser beam after *N*pulses [7],

$$T(x, y, z, t) = \sum_{n=0}^{N} T^{s.p.}(x, y, z, t + n\Delta t_{p-p}), \tag{5}$$

where t_{p-p} is the time between consecutive laser pulses and the temperature induced by a single laser pulse $T^{s.p.}$ is given by [7],

$$T^{s.p.}(x, y, z, t) = \frac{2E_{res}}{\pi\rho C_p\sqrt{\pi\kappa t}\,(8\kappa t + \omega_0^2)} \cdot e^{\frac{(x-x_c)^2+(y-y_c)^2}{4\kappa t}\left(\frac{\omega_0^2}{8\kappa t+\omega_0^2}-1\right)} \cdot e^{-\frac{z^2}{4\kappa t}}, \tag{6}$$

where (x_c, y_c) are center coordinates of the laser spot, ρ, C_p, κ and ω_0 are density, specific heat capacity, thermal diffusivity of the material and beam radius respectively. Here, the residual energy E_{res} is the product of incident pulse energy E_p and the residual rate of single pulse energy η_{res} [36]. In this paper, we model this η_{res} as

$$\eta_{res} = \frac{AE_p - \rho\Delta V L_{vap}}{E_p} \times 100\%, \tag{7}$$

where L_{vap} is the latent heat of vaporization and ΔV is the volume ablation rate per pulse. From the confocal data, ΔV is calculated as the ablated volume at a given number of pulses divided by the number of laser pulses. The maximum ablated depth per pulse measured from the confocal data serves as *z*values in Eq. (6). In case of galvanized steel, we used the material parameters of Zn when $z \leqslant 10$ μm, and of forming steel when $z > 10$ μm. The interface between the coating and the substrate was assumed to be continuous, i.e. $T^{Zn}(x, y, z, t) = T^{Steel}(x, y, z, t)$ at $z = 10$ μm. Note that, this numerical heat flow model is simplified extensively, i.e. (a) except for Eq. (7), latent heat of melting and vaporization were not taken into account during the temperature rise, (b) heat flow is unidirectional, i.e. no heat flows from the substrate to the Zn coating layer, nor from the surface to the surrounding, and (c) ablated depth is removed as a plane without following the actual curvature of the crater. These simplifications result

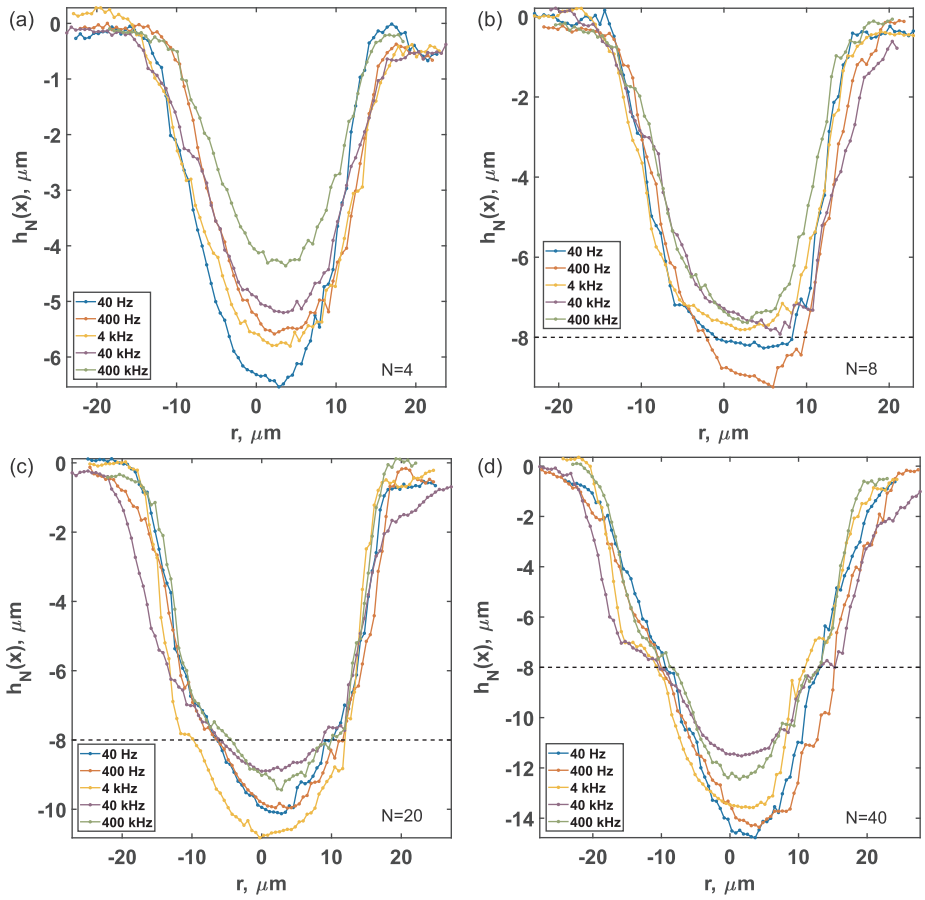

Fig. 8. Cross-sections (obtained from CLSM measurements) of ablated craters on galvanized steel surface normalized by corresponding number of pulses *N*at $F_0 = 40$ J/cm^2 and a wavelength of 515 nm. The dashed horizontal line in the graphs represents the nominal interface between the Zn coating and steel substrate.

in higher estimation of $T(x, y, z, t)$ than the actual temperature.

Fig. 9 shows simulation results of $T(0, 0, z, t)$ for bulk and coated zinc samples processed at $N = 40$ and $F_0 = 40$ J/cm^2. Fig. 9 (a)-(c) demonstrates the temperature increase of bulk zinc processed at a wavelength of 1030 nm and at $E_p = 135$ µJ. On the other hand, Fig. 9 (d)-(e) shows the temperature increase of galvanized steel processed at a wavelength of 515 nm and at $E_p = 82$ µJ. As can be concluded from Fig. 9(a) for Zn sample at $N = 40$, the sample temperature increases as the time between consecutive pulses decreases due to the residual energy of the previous pulses. In this figure, the rise in residual temperature is shown for the surface without compensating for ablated depth per pulse, i.e. $z = 0$ in Eq. (5). The temperature increase is negligible, and below 80 K up to $f_p = 40$ kHz (all curves except the green curve). However, at 400 kHz, zinc heats up due to the residual heat from room temperature to melting point after 2 pulses (shown by the dashed horizontal line) and exceeds vaporization temperature after 8 pulses (shown by the dashed-dotted horizontal line) for $N = 40$ as shown in Fig. 9(a). A closer view at 400 kHz and 40 Hz with compensation for ablated depth per pulse, shown in Fig. 9(b) and (c) respectively, shows the build up of temperature at different depths over time. As can be observed from these figures, the temperature increase at different depths is negligible when the time between consecutive pulses is long i.e. longer than 1 ms (see Fig. 9(c)). Also a saturation in ΔT over time can be observed. On the contrary, the differences in ΔT at subsequent depth levels become significant at 400 kHz and the saturation in ΔT is absent for $N = 40$ (see Fig. 9(b)). Although a crude approximation, it follows from Fig. 9(a) that the ablation process of zinc is significantly affected by the presence of melt layer in multiple pulse processing, when the time between consecutive pulses is less than 25 µs. This approximation is further backed by the presence of rim around the crater at 400 kHz (see Fig. 1(i)) over the HAZ at 4 kHz (see Fig. 1(f)). Generally, it is known that the reflectivity of metals decreases with increasing temperature [37]. Therefore, absorption as well as energy penetration depth increases as the sample temperature increases. The latter is not incorporated in our model. Since the sample temperature difference at $N = 4$ is not as high as $N = 40$, the increase in energy penetration depth is not significant, as is shown in Fig. 2(b). With increasing number of pulses on the same location, a higher recoil pressure (from the ablated species) on the molten zinc pushes melt outwards, creates a deeper crater as well as higher rim at 400 kHz than other repetition rates (see Fig. 4).

In case of Zn-coated steel, i.e. galvanized steel, the effect of substrate on the coating layer is significant; although, a coating layer thickness of about 10 µm is sufficiently thick to exclude it as a thin film. Moreover, optical penetration depth of zinc at a wavelength of 515 nm is about 15 nm, which is two order of magnitude smaller than the coating thickness. Fig. 9(d) and (e) illustrates the simulation results of Eq. (5) for galvanized steel samples. As can be observed from Fig. 9(e), substrate steel heats up 4 times more (quickly) than the zinc coating, whereas the heating behavior of the zinc coating is similar to bulk zinc as shown in Fig. 9(c). The effect of substrate on the temperature becomes prominent at higher repetition rate as can be observed in Fig. 9(d). In this figure, the dashed and dashed-dotted horizontal lines represent the melting and vaporization temperature T_v of zinc (black) and iron (red) curve. Unlike bulk Zn, the zinc coating does not heat up above T_v. This might result from lower absorptivity of Zn at 515 nm than 1030 nm. Moreover, the considerably higher degree of heating in substrate steel indicates that the substrate acts as a heat sink for the heat in the coating. Therefore, less melt is formed, which results in little to no rim around the crater (see Fig. 5)).

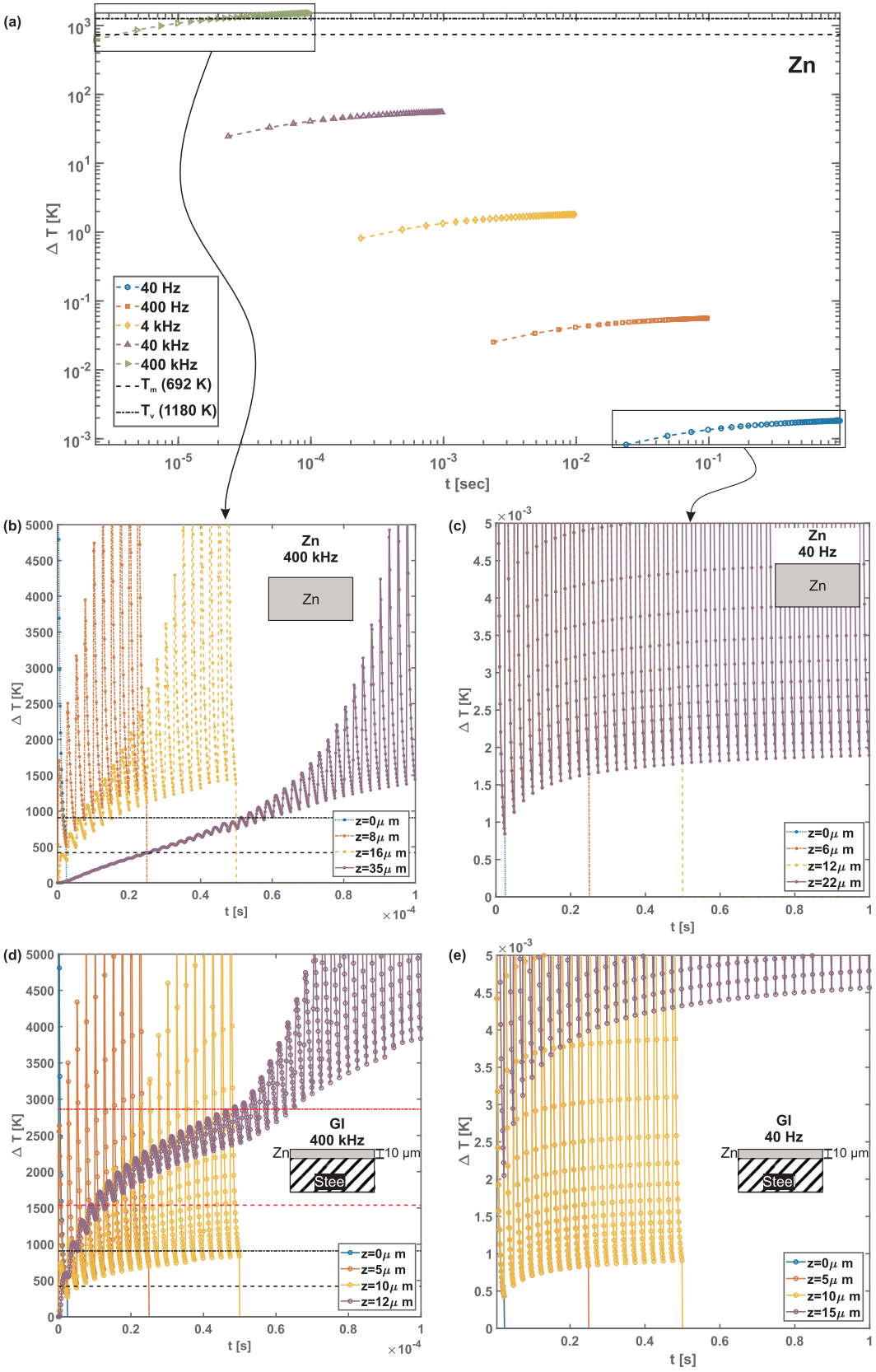

Fig. 9. (a) Simulation of the difference of the maximum temperature increase induced by a stationary laser beam at different pulse repetition rates for bulk zinc processed at $\lambda = 1030$ nm, $E_p = 135$ μJ and $N = 40$. Evolution of ΔT with processing time for bulk zinc processed at (b) 400 kHz and (c) 40 Hz. Evolution of ΔT with processing time for galvanized steel processed at $\lambda = 515$ nm, $E_p = 82$ μJ and at (d) 400 kHz and (e) 40 Hz.

Since galvanized steel is an engineering material, the (relatively) high surface roughness of the coating layer ($R_a < 0.5$ μm) and the substrate steel ($R_a < 1.6$ μm) also affects the laser processing at a wavelength of 515 nm [25]. As a consequence, the differences in ΔV at low number of pulses is not that significant and the uncertainty in fit parameters (F_{th} and δ_e) is larger (see Fig. 6). Since substrate steel acts as a heat sink, the dominance of heat accumulation over particle shielding is not observed in the maximum crater depth in Zn-coated steel (see Fig. 7(a)). Inspite of lower crater depth, MRR increases with increasing pulse repetition rate (see Fig. 7(a)), because the crater wall gets steeper in coating layer with increasing f_p (see Fig. 8).

In general, as the time between consecutive pulses gets shorter with increasing pulse frequency, heat accumulation becomes conducive to material removal rate, while the maximum achievable depth gets limited by particle shielding of the laser beam. In the case of processing bulk zinc at 1030 nm, heat accumulation subjugates particle shielding at high repetition rate, resulting in significant increase in ablated depth and volume, while being detrimental to processing quality. On the contrary, the maximum achievable depth in galvanized steel, processed at 515 nm, with increasing repetition rate is restricted by particle shielding, since the steel substrate hinders heat accumulation in the coating layer by acting as a heat reservoir. Also, Zn-coated steel exhibits imperceptible differences in processing quality at the investigated repetition rates, with higher MRR for higher repetition rates. Therefore, from a process upscaling point of view, high repetition rate for processing galvanized steel is preferred. For processing bulk zinc, a balance between processing quality and MRR is required.

5. Conclusion

Within the boundary of our experimental conditions, bulk and coated zinc behaves differently with increasing pulse repetition rate. However, in both cases, material removal rate increases with increasing pulse frequency, and the differences in threshold fluence and energy penetration depth at low number of pulses is negligible. The maximum achievable depth decreases with increasing pulse repetition rate due to shielding of the laser beam by ablated particles. For bulk zinc, heat accumulation at high repetition rate (400 kHz) dominates over particle shielding, resulting in higher ablated depth and volume at the cost of lower processing quality. A numerical heat flow model revealed a high degree of sample heating from the residual energy of previous pulses. In the case of a zinc coating on steel, the steel substrate acts as a heat sink preventing higher degree of heat accumulation in the coating layer, when compared to bulk zinc. Taking the maximum achievable depth, material removal rate and processing quality into consideration, a trade-off between quality and removal rate is required for processing bulk zinc, whereas high repetition rate is preferred for processing zinc-coated steel.

Declaration of Competing Interest

None.

Acknowledgment

The authors would like to acknowledge the financial support of Tata Steel Nederland Technology BV. We would also like to thank Dr. W. Ya and Dr. B. Pathiraj of the University of Twente for their fruitful discussions on this topic.

References

[1] K. Sugioka, Progress in ultrafast laser processing and future prospects, Nanophotonics 6 (2017) 393–413.
[2] Q. Ding, L. Wang, L. Hu, Tribology optimization by laser surface texturing: from bulk materials to surface coatings, Elsevier, 2015, pp. 405–422.
[3] G. Račiukaitis, M. Brikas, P. Gecys, B. Voisiat, M. Gedvilas, et al., Use of high repetition rate and high power lasers in microfabrication: how to keep the efficiency high? JLMN J. Laser Micro/Nanoeng. 4 (2009) 186–191.
[4] B. Neuenschwander, G.F. Bucher, G. Hennig, C. Nussbaum, B. Joss, M. Muralt, S. Zehnder, U.W. Hunziker, P. Schütz, Processing of dielectric materials and metals with ps laser pulses, Int. Congr. Appl. Lasers Electro-Opt. 2010 (2010) 707–715.
[5] B. Jaeggi, B. Neuenschwander, S. Remund, T. Kramer, Influence of the pulse duration and the experimental approach onto the specific removal rate for ultrashort pulses, in: Laser Applications in Microelectronic and Optoelectronic Manufacturing (LAMOM) XXII, volume 10091, International Society for Optics and Photonics, 2017, p. 100910J.
[6] J. Schille, L. Schneider, P. Lickschat, U. Loeschner, R. Ebert, H. Exner, High-pulse repetition frequency ultrashort pulse laser processing of copper, J. Laser Appl. 27 (2015) S28007.
[7] F. Bauer, A. Michalowski, T. Kiedrowski, S. Nolte, Heat accumulation in ultra-short pulsed scanning laser ablation of metals, Opt. Exp. 23 (2015) 1035–1043.
[8] J. König, S. Nolte, A. Tünnermann, Plasma evolution during metal ablation with ultrashort laser pulses, Opt. Exp. 13 (2005) 10597–10607.
[9] A. Ancona, F. Röser, K. Rademaker, J. Limpert, S. Nolte, A. Tünnermann, High speed laser drilling of metals using a high repetition rate, high average power ultrafast fiber CPA system, Opt. Exp. 16 (2008) 8958–8968.
[10] A. Ancona, D. Nodop, J. Limpert, S. Nolte, A. Tünnermann, Microdrilling of metals with an inexpensive and compact ultra-short-pulse fiber amplified microchip laser, Appl. Phys. A 94 (2009) 19–24.
[11] R. Benocci, D. Batani, H.E. Roman, Incubation models for under-threshold laser ablation with thermal dissipation, Appl. Phys. B 125 (2019) 22.
[12] F. Di Niso, C. Gaudiuso, T. Sibillano, F.P. Mezzapesa, A. Ancona, P.M. Lugarà, Role of heat accumulation on the incubation effect in multi-shot laser ablation of stainless steel at high repetition rates, Opt. Exp. 22 (2014) 12200–12210.
[13] S. Biswas, A. Karthikeyan, A.-M. Kietzig, Effect of repetition rate on femtosecond laser-induced homogenous microstructures, Materials 9 (2016) 1023.
[14] F. Fraggelakis, G. Mincuzzi, J. Lopez, I. Manek-Hönninger, R. Kling, Texturing metal surface with mhz ultra-short laser pulses, Opt. Exp. 25 (2017) 18131–18139.
[15] S.M. Eaton, H. Zhang, P.R. Herman, F. Yoshino, L. Shah, J. Bovatsek, A.Y. Arai, Heat accumulation effects in femtosecond laser-written waveguides with variable repetition rate, Opt. Exp. 13 (2005) 4708–4716.
[16] J. Finger, C. Kalupka, M. Reininghaus, High power ultra-short pulse laser ablation of IN718 using high repetition rates, J. Mater. Process. Technol. 226 (2015) 221–227.
[17] J. Schille, L. Schneider, U. Loeschner, Process optimization in high-average-power ultrashort pulse laser microfabrication: how laser process parameters influence efficiency, throughput and quality, Appl. Phys. A 120 (2015) 847–855.
[18] B. Jaeggi, B. Neuenschwander, M. Zimmermann, L. Penning, K. Weingarten, A. Oehler, et al., High-throughput and high-precision laser micromachining with ps-pulses in synchronized mode with a fast polygon line scanner, in: Laser Applications in Microelectronic and Optoelectronic Manufacturing (LAMOM) XIX, volume 8967, International Society for Optics and Photonics, 2014, p. 89670Q.
[19] J. Lopez, G. Mincuzzi, K. Mishchik, E. Audouard, E. Mottay, R. Kling, Correlation between ablation efficiency, surface morphology, and multipass capability using a 100-W 10-MHz ultrafast laser, in: Laser Applications in Microelectronic and Optoelectronic Manufacturing (LAMOM) XXIII, volume 10519, International Society for Optics and Photonics, 2018, p. 1051909.
[20] M. Sailer, F. Bauer, J. Kleiner, M. Kaiser, Scaling of ablation rates. ablation efficiency and quality. aspects of burst-mode micromachining of metals, in: presented at Laser in Manufacturing Conference, 2015.
[21] B. Jaeggi, S. Remund, R. Streubel, B. Goekce, S. Barcikowski, B. Neuenschwander, Laser micromachining of metals with ultra-short pulses: factors limiting the scale-up process, J. Laser Micro/Nanoeng. 12 (2017).
[22] I. Daigo, S. Osako, Y. Adachi, Y. Matsuno, Time-series analysis of global zinc demand associated with steel, Resour. Conserv. Recycl. 82 (2014) 35–40.
[23] U.S. Geological Survey, Mineral Commodity Summaries 2013, 2013. doi:10.3133/70202434, p.188–189.
[24] H. Mustafa, R. Pohl, T.C. Bor, B. Pathiraj, D.T.A. Matthews, G.R.B.E. Römer, Picosecond-pulsed laser ablation of zinc: crater morphology and comparison of methods to determine ablation threshold, Opt. Exp. 26 (2018) 18664–18683.
[25] H. Mustafa, D.T.A. Matthews, G.R.B.E. Römer, Investigation of the ultrashort pulsed laser processing of zinc at 515 nm: Morphology, crystallography and ablation threshold, Mater. Des. 107675 (2019).
[26] J. Xiao, P. Liu, C.X. Wang, G.W. Yang, External field-assisted laser ablation in liquid: an efficient strategy for nanocrystal synthesis and nanostructure assembly, Prog. Mater Sci. 87 (2017) 140–220.
[27] I. Nicolae, M. Bojan, C. Viespe, D. Miu, Repetition rate effects in picosecond laser microprocessing of aluminum and steel in water, Micromachines 8 (2017) 316.
[28] C. Gaudiuso, H. Kämmer, F. Dreisow, A. Ancona, A. Tünnermann, S. Nolte, Ablation of silicon with bursts of femtosecond laser pulses, in: Frontiers in Ultrafast Optics: Biomedical, Scientific, and Industrial Applications XVI, volume 9740, International Society for Optics and Photonics, 2016, p. 974017.
[29] H. Kämmer, F. Dreisow, A. Tünnermann, S. Nolte, Analysis of the hole shape evolution in fs-pulse percussion drilling with bursts, in: Frontiers in Ultrafast Optics: Biomedical, Scientific, and Industrial Applications XVI, volume 9740, International Society for Optics and Photonics, 2016, p. 974012.
[30] B. Wu, L. Deng, P. Liu, F. Zhang, J. Duan, X. Zeng, Effects of picosecond laser repetition rate on ablation of Cr12MoV cold work mold steel, Appl. Surf. Sci. 409 (2017) 403–412.
[31] J. Mur, J. Petelin, N. Osterman, et al., High precision laser direct microstructuring system based on bursts of picosecond pulses, J. Phys. D: Appl. Phys. 50 (2017)

325104.
[32] MATLAB, version 9.3.0.713579 (R2017b), The MathWorks Inc., Natick, Massachusetts, 2017.
[33] G. Raciukaitis, M. Brikas, P. Gecys, M. Gedvilas, Accumulation effects in laser ablation of metals with high-repetition-rate lasers, in: High-Power Laser Ablation VII, volume 7005, International Society for Optics and Photonics, 2008, p. 70052L.
[34] T. Kramer, S. Remund, B. Jäggi, M. Schmid, B. Neuenschwander, Ablation dynamics–from absorption to heat accumulation/ultra-fast laser matter interaction, Adv. Opt. Technol. 7 (2018) 129–144.
[35] A. Vorobyev, C. Guo, Direct observation of enhanced residual thermal energy coupling to solids in femtosecond laser ablation, Appl. Phys. Lett. 86 (2005) 011916.
[36] B. Wu, P. Liu, X. Wang, F. Zhang, L. Deng, J. Duan, X. Zeng, Effect of laser absorption on picosecond laser ablation of Cr12MoV mold steel, 9Cr18 stainless steel and H13A cemented carbide, Opt. Laser Technol. 101 (2018) 11–20.
[37] K. Ujihara, Reflectivity of metals at high temperatures, J. Appl. Phys. 43 (1972) 2376–2383.